IJMT. Vol. 23, Iss. 1, 202. (99-116)

International Journal of Maritime Technology

Journal homepage: ijmt.ir

Comparative Hydraulic Performance of Conceptual Breakwater Armor Geometries under Changing Sea States: Effects of Sea-Level Rise and Irregular Waves

Mohammad Taghipour[1], Reza Dezvareh[2]*, Nosratollah Falah[3]

[1] *MSc Student, Faculty of Civil Engineering, Babol Noshirvani University of Technology, Babol, Iran.Babol Noshirvani University of Technology, Babol, Iran, mohammadtaghipour1378@gmail.com*

[2] *Associate Professor, Faculty of Civil Engineering, Babol Noshirvani University of Technology, Babol, Iran.Babol Noshirvani University of Technology, Babol, Iran, rdezvareh@nit.ac.ir*

[3] *Professor, Faculty of Civil Engineering, Babol Noshirvani University of Technology, Babol, Iran.Babol Noshirvani University of Technology, Babol, Iran, fallah@nit.ac.ir*

ARTICLE INFO

Article History:
Received:
Last modification:
Accepted:
Available online:

Article type:
Research Paper

Keywords:
Rubble-mound breakwater
Concrete armor unit
Sea-level rise
JONSWAP spectrum
Wave overtopping

ABSTRACT

Climate-change-driven sea-level rise reduces breakwater freeboard and can permit larger wave groups to reach the structure before depth-induced breaking occurs, thereby increasing run-up and overtopping. This study evaluates the hydraulic resilience of two conceptual concrete armor geometries: a symmetric unit (Type A1; 1:1 aspect ratio) and an elongated unit (Type A2; 1:2 aspect ratio). Six rubble-mound breakwater configurations (B1-B6), combining slopes of 1:1.5 and 1:2.0 with regular or irregular placement, were represented as fixed geometries in FLOW-3D. The numerical model used three-dimensional Reynolds-averaged Navier-Stokes equations, an RNG k-ε closure, volume-of-fluid free-surface tracking, FAVOR geometry representation, and a porous-core formulation. Irregular incident waves were generated from a normalized JONSWAP spectrum with significant wave heights of 1.6 and 1.8 m, a peak period of 6.0 s, and still-water depths of 3.3, 3.8, and 4.3 m. Model performance was checked against published overtopping data. A local-maximum crest-exceedance analysis and empirical crest-exceedance response curves were used to quantify the hydraulic response across the modeled water levels; this hydraulic limit state does not represent physical armor displacement or breakage. Across the six configurations, the +1.0 m water-level scenario increased exceedance probability by 21-57 percentage points relative to baseline. When averaged across the two modeled significant wave heights, B3 (irregular A2, slope 1:1.5) increased from 35% to 92%, whereas B1 (regular A1, slope 1:1.5) increased from 15% to 38%. The response is consistent with greater flow-path tortuosity in the symmetric layer and preferential channeling in irregular elongated arrangements. Screening-level Hudson mass corrections indicate substantially larger adaptation demands for A2. Because the armor units were fixed and the probabilities were derived from finite numerical records at three water levels, the results should be interpreted as comparative hydraulic screening metrics rather than annual failure probabilities or structural service-life predictions.

ISSN: 2645-8136

DOI:

1. Introduction

The use of rubble-mound breakwaters is of significant importance to ports and exposed coastlines since these structures can lower the energy of incoming waves thus ensuring safety for navigational areas, terminals, and coastal infrastructure. Their effectiveness is highly dependent on the main layer of protection made of quarried rocks or especially pre-shaped concrete structures [1]. An initial design includes the hydraulic behavior of the structure, its performance, and the tolerable limit of overtopping. Historic evolution of concrete armor involves finding the optimal solution to the problem of unit weight, interlocking, porosity, construction, and energy dissipation [2-4]. Design calculations in the early stage of the project are usually based on the Hudson's relationship as far as stability and overtopping for irregular waves are calculated using Van der Meer and EurOtop techniques [1,5]. Even though the mentioned methods are important, their empirical coefficients appear to be impossible to interpret correctly under the changed water level, storm action, and state of the structure.

According to the Intergovernmental Panel on Climate Change, the average sea level is rising more quickly, and extreme sea level events have increased in frequency along many coastlines [6]. In case of a pre-existing breakwater, as the still water level rises, the effective crest freeboard decreases as well as the water depth at the toe. The deeper waves can travel closer to the structure before breaking, causing the shifting of energy dissipation away from the foreshore area and toward the armor slope and crest of the structure. This does not mean that every wave is higher than the previous one; it means that a specific wave has changed its breaking pattern as a result of the rising sea level.

The assessment of the breakwater performance in the 21st century should incorporate irregular wave modeling instead of relying solely on monochromatic waves. The statistics of ocean waves and random phases lead to the genesis of wave groups [7,8]. Both reflected spectra and incident spectra can be differentiated by means of well-established multi-probe methods [9]. Spatial studies reveal that overtopping is highly inhomogeneous along complex armor and berm systems [10]. The three-dimensional RANS-VOF modeling makes it possible to reproduce essential aspects of wave run-up and overtopping processes concerning rubble mound breakwaters and thus to be a helpful complement to both physical modeling and empirical formulas [11-16]. Nevertheless, the accuracy of the numerical model should be considered because it depends on the mesh, turbulence closure, porous flow treatment, wave generation methods, and the absorbers used. The requirements are critically essential for probability calculations based on irregular wave files.

Against this background, the present study compares two conceptual concrete armor geometries while holding the principal environmental forcing and unit mass constant: Type A1 is symmetric with an aspect ratio of 1:1, whereas Type A2 is elongated with an aspect ratio of 1:2. Six configurations, designated B1-B6, combine these geometries with slopes of 1:1.5 and 1:2.0 and with regular or irregular placement. The objectives are to: (1) generate repeatable irregular wave trains from a JONSWAP spectrum; (2) quantify how +0.5 and +1.0 m still-water-level increments modify crest-exceedance behavior; (3) compare empirical crest-exceedance response curves for the symmetric and elongated arrangements; and (4) examine screening-level adaptation indicators, including residual hydraulic margin and Hudson-based compensatory mass. The comparison relates to the hydraulic limit state of functionality. The model does not address issues related to armor movement, rocking, collision, breaking of concrete, or progressive mechanical damage. Analysis of non-stationary coastal hazard is carried out through the interplay between changing water levels and frequency of extreme events. Within the stationary design framework, estimation of the moment of return is performed with the assumption of its invariability over time. As the relative sea level rises, however, the elevation threshold determining the occurrence of damaging storm surge becomes exceeded more frequently even though the offshore wave climate remains the same. According to the Intergovernmental Panel on Climate Change, extreme sea levels that were historically expected to occur once a century will happen at many locations with tide gauges at least once a year by 2100 [6]. The same principle applies to a breakwater which leads to reduction of freeboard available for containing run-up and overtopping. Hence, safety factors estimated based on historic water levels cannot be regarded as ensuring the same level of functional reliability throughout the decades of service.

The random nature of overtopping adds another dimension to the analysis of overtopping. On top of average discharge, the average value of the discharge, q, remains a key measure of serviceability in the EurOtop guidance but it is also necessary to take into account the specific strong discharge events occurring on individual occasions [5]. A string of large waves can be seen even before the porous armor and the core have been fully drained, which will enable the second or the third wave to be more powerful than the first even though the height of the largest wave remains constant. To this end, the study uses the peaks-over-threshold (POT) method to keep the records of the waves that exceed the limit state and to compare how often and how powerful those instances were according to the configuration used.

The historical context of concrete armor can be extremely useful in understanding the comparison of aspect ratio. The first concrete armor designs like cubes, Tetrapods and Antifer units were developed but the performance still highlights the significance of the unit placement, forces exerted and local stress conditions [2,3]. Later developments like Accropode, Core-Loc and Xbloc families, were developed to improve hydraulic stability through the manipulation of placing and geometry [4,17,18]. The studies of recent times were based on the understanding of the hydrodynamics of armor [19,20]. The even very fact of converting the regular unit of concrete into an elongate force, brings to incompleteness of the study about its hydraulic consequences, especially in case of achieving irregularity in the unit placement and no freeboard position of the unit.

The handling of boundary reflection is essential for irregular-wave simulation for longer durations. The short-wave reflection, together with the bound long-wave components, has the potential to pollute incident frequency, generate false standing waves, and alter overtopping statistics [21]. While FLOW-3D offers the technology for wave generation and absorption, other numerical packages involve methods based on domain decomposition and relaxation zones [22]. In the present study, the active absorption was performed at the boundaries with using the same tone of random-phase realization in the experiment. The method guarantees higher comparison continuity, however for the estimation of error, different phase seeds have to be obtained.

In terms of port functionality, too much overtopping can interfere with loading/unloading operations, risk workers and vehicles, inundate road surfaces and utilities, speed up corrosion, and cause damage to back protection. In this regard, overtopping guidelines have evolved from initial requirements for seawalls designed based on discharge to modern tolerance limits related to risk [5]. Results of the effect depend on the state of environment behind the crest; hence, there is no universal discharge level of overtake for breakwaters. Furthermore, crest elevation is used as a reference value rather than as a method for risk assessments. In fact, proper design should utilize hydraulic pressures in order to evaluate possible discharges, drainage facilities, resistance of rear slopes, accessibility, and downtime of the port.

Earlier computational analyses revealed that armor types, positioning, and breakwater form can affect wave run-up and overtopping; yet there has been less clarity over their enhanced effect in low freeboard contexts. This research seeks to fill this gap by conducting controlled numerical experiments that allow for the exploration of the various effect of armor mass, incoming wave characteristics, and varying random-phase realization against the other aspects in a range of scenarios such as armor aspect ratio, armor placement, slope of breakwater, and still-water level. Therefore, the focus of the research will be to compare different forms of armor. Traditional analytical wave approaches and empirical formulae for overtopping are good for preliminary designs and assessments. However, they fail to capture all the three-dimensional interactions occurring during the breaking process, such as the breaking waves, the empty armor, the entrapped air, the infiltration in the porous material, and the crest flow [1,7]. RANS-VOF makes some progress in addressing this challenge by solving the free surface and the mean turbulence around complex immovable geometry. Increased spatial accuracy, however, does not eliminate uncertainties in the calculations as it is still important to properly specify grid resolution, interface compression, turbulence closure, roughness, the coefficients of porosity, and numerical dissipation. Therefore, this paper is using CFD as a comparative flume and considers its output as scenario specific hydraulic information and not as an ultimate proof of resistance of the system.

Previous studies have demonstrated the impact of armor type, positioning, and breakwater design on run-up and overtopping, while the newly developed numerical simulations have offered useful insights about water flow through the armor. However, the literature lacks any controlled information on the relationships between armor aspect ratio and arrangement and the gradual lowering of freeboard when passing identical irregular waves. This paper intends to fill this gap by comparing symmetrical and elongated armor configurations in the same RANS–VOF, changing breakwater slope and still-water elevation at the same time.

In this context, this paper develops a framework for controlled comparisons in order to separate the effects of armor aspect ratio, arrangement, breakwater slope, and decrease in freeboard during irregular JONSWAP forcing.

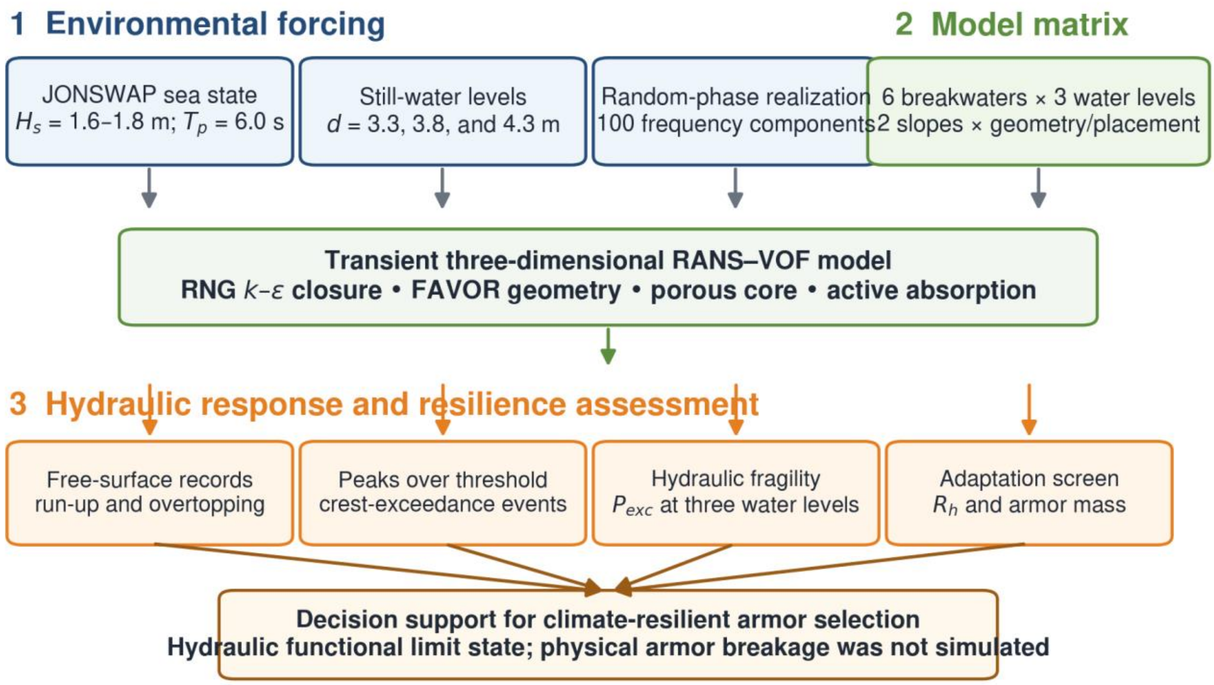

Figure 1. Climate-resilience workflow linking environmental forcing, the six-configuration CFD matrix, and hydraulic-response screening.

2. Materials and Methods

A transient three-dimensional numerical model was developed in FLOW-3D to simulate the interaction between irregular waves and a breakwater cross-section [21]. The Reynolds-averaged Navier-Stokes equations were used to analyze the incompressible flow field. A turbulent stress term was included in the analysis using the RNG k-ε model, while the volume-of-fluid (VOF) method was employed for tracking the water-air surface. The VOF method employs a fractional-volume formulation for free surfaces [23], while structurs is modeled with the help of the FAVOR porosity approach [24]. The use of the RNG closure introduces strain-effects into the dissipation equation, which is particularly suitable for rapid strains and flows involving free surfaces [25].

The numerical program was composed as a controlled comparative matrix, where the primary variables were incident wave height, still-water height, armor structure geometry, position arrangement, and slope of breakwater. There were two significant wave heights equal to H_s= 1.6 and 1.8 m combined with three still-water heights of 3.3, 3.8, and 4.3 m representing three different scenarios of the baseline, +0.5 m, and +1.0 m. These conditions were applied for configurations B1 to B6 without deviations. All simulations were characterized with the same peak period, spectral formulation, random phase realization, porous material characteristics, and numerical system so that the differences in hydraulic performance could be explained by the variation in geometry, positioning, slope, wave height and free board depending on what.

The irregular incident waves were generated numerically by a wavemaker utilizing the JONSWAP spectral density function. Each realize was composed of 100 frequency components with fixed random phases. In reality, it retains the same phase for paired simulations so that any variation in armor configurations does not interfere with the different incident history. Active absorption was adopted to overcome re-reflections from the boundaries. After the desired surface-elevation record was generated, it was compared with the target spectrum and the significant wave height. Although this technique generates repeatable wave grouping and extremely large crests in a finite record, it cannot reproduce rogue-wave phenomenon or provide a full probability distribution of all the necessary phase realizations.

2.1. Spectral Wave Forcing: The JONSWAP Formulation

The one-dimensional JONSWAP spectrum was used in its standard frequency-domain form. In Eq. (1), α is a scale coefficient, g is gravitational acceleration, f_p is the peak frequency, γ is the peak-enhancement factor, and σ equals 0.07 for $f \leq f_p$ and 0.09 for $f > f_p$. The exponent r concentrates energy near the spectral peak. Rather than adopting an arbitrary α value, the discretized spectrum was normalized so that its zeroth moment reproduced the prescribed significant wave height. The random-phase surface elevation was then synthesized using Eq. (2), where Δf_i is the width of frequency band i and φ_i is its fixed phase angle. This normalization makes the spectral area, rather than only the plotted peak, consistent with H_s.

$$S(f) = \alpha g^2(2\pi)^{-4} f^{-5} exp[-1.25(f_p/f)^4]\gamma^r, r = exp[-(f-f_p)^2/(2\sigma^2 f_p{}^2)] \quad (1)$$

$$\eta(t) = \Sigma_{i=1}{}^N[2S(f_i)\Delta f_i]^{1/2} cos(2\pi f_i t + \varphi_i) \quad (2)$$

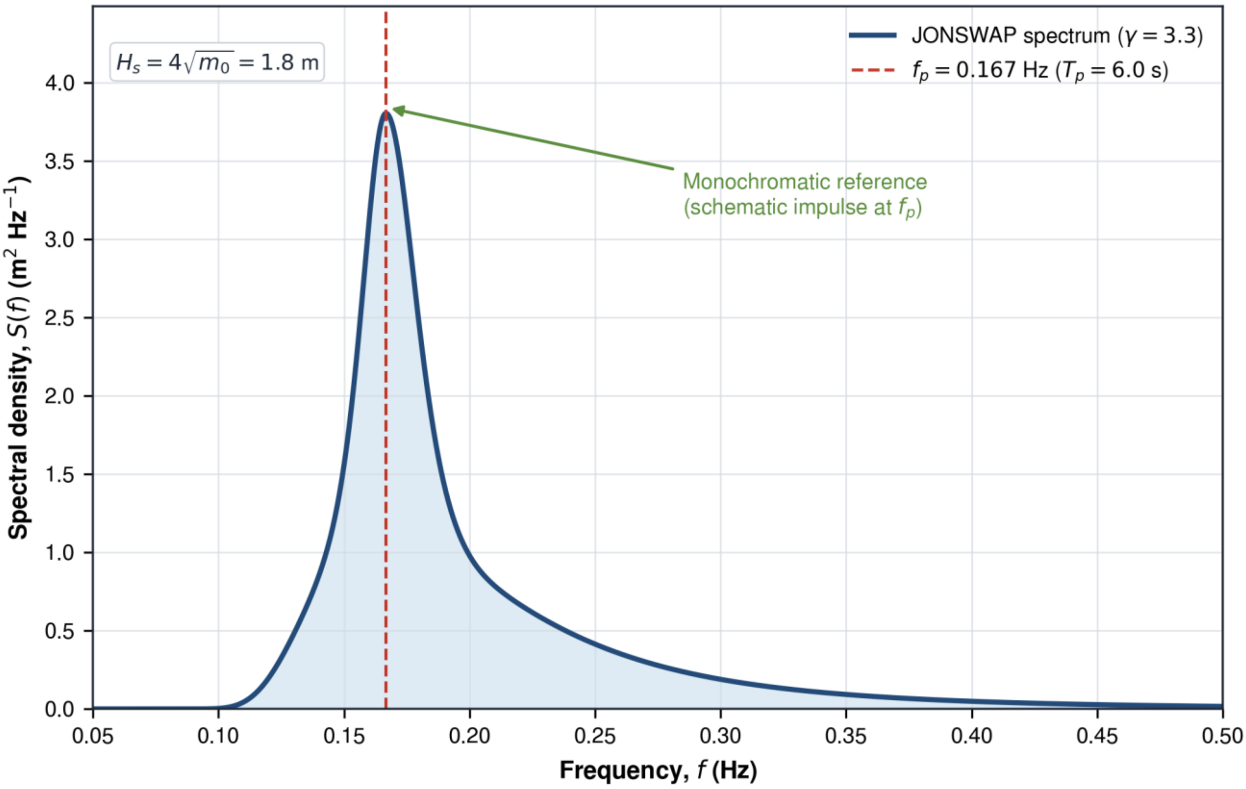

Figure 2. Normalized JONSWAP spectral density for Hs = 1.8 m and Tp = 6.0 s; the monochromatic reference is shown schematically as an impulse at fp.

2.2. Statistical Wave Parameters

Sea-state severity was characterized through spectral moments. The nth moment is $mn = integral(f^n S(f)df)$; therefore $Hs = 4sqrt(m0)$, and the peak period is Tp = 1/fp. Two incident significant wave heights were examined, Hs = 1.6 and 1.8 m, with Tp = 6.0 s. Three still-water depths represented the water-level scenarios: 3.3 m at baseline, 3.8 m for +0.5 m sea-level rise, and 4.3 m for +1.0 m sea-level rise. The breakwater crest elevation was 5.0 m, giving effective freeboards of 1.7, 1.2, and 0.7 m, respectively. The sea-level-rise increments are scenario values imposed on the numerical domain and should not be interpreted as site-specific projections without a local datum, vertical-land-motion assessment, and planning horizon.

$$m_n = \int_0 \infty f^n S(f)df, H_s = 4\sqrt{m_0}, T_p = 1/f_p \quad (3)$$

The environmental forcing matrix is illustrated through Table 1, which indicates six combinations of incident wave height and still-water depth. Each combination from the table was applied to the breakwater configurations consistently. All paired cases had the same peak period and phase realization, thereby allowing isolating the effect of the variation in wave height, freeboard, slope, aspect ratio of the armor, and the position of the breakwater. It is recommended to use more phase seeds because this will enable making a broader statistical sample for the uncertainty quantification.

Table 1. Environmental forcing matrix used for the two incident wave heights and three still-water levels.

Wave condition	Significant wave height, H_s (m)	Peak period, T_p (s)	**Still-water depth, d (m)**
Moderate storm - baseline	1.6	6.0	3.3
Limit-state storm - baseline	1.8	6.0	3.3
Moderate storm - +0.5 m SLR	1.6	6.0	3.8
Limit-state storm - +0.5 m SLR	1.8	6.0	3.8
Moderate storm - +1.0 m SLR	1.6	6.0	4.3

Wave condition	Significant wave height, H_s (m)	Peak period, T_P (s)	**Still-water depth, d (m)**
Limit-state storm - +1.0 m SLR	1.8	6.0	4.3

2.3. Numerical Domain, Configurations, and Sea-Level-Rise Scenarios

Six types of breakwater configurations were utilized in the environmental cases. The configurations B1 and B4 employed standard symmetrical armor type A1 on slopes of 1:1.5 and 1:2.0, respectively. The configurations B2 and B5 employed standard elongated type armor A2 on the same slopes as above. Finally, the configurations B3 and B6 used irregular standard armor type A2. The configurations had the same design weight of 3,030 kg calculated by using Hudson's approach. The geometry was predetermined in the CFD computations, and thus the approach is used to study hydrodynamic response only, and the assessment of incipient motion and stability of structures cannot be determined. The CFD model consisted of approximately 1.41 million control volumes created by the multi-block mesh technique. The smallest control volume is equal to 0.05m.

The scenario matrix was chosen so that it could serve as a complete and defined evaluation of the primary hydraulic parameters without serving as an indicator of an actual site in the future. There were two heights of wave in the experiment, that is H_s=1.6 and 1.8 m. The period $T_p = 6.0s$ was kept uniform throughout the experiment to eliminate the possibility of introducing additional effects due to the period of waves. Wave heights of 3.3, 3.8, and 4.3 m correspond to the baseline, +0.5 m, and +1.0 m conditions respectively thus allowing the effective freeboard to be decreased respectively from 1.7m to 1.2m and then to 0.7m. The configurations in B1 to B6 were selected so that aspects like ratio, method of placement, and slope could be compared in the experiment.

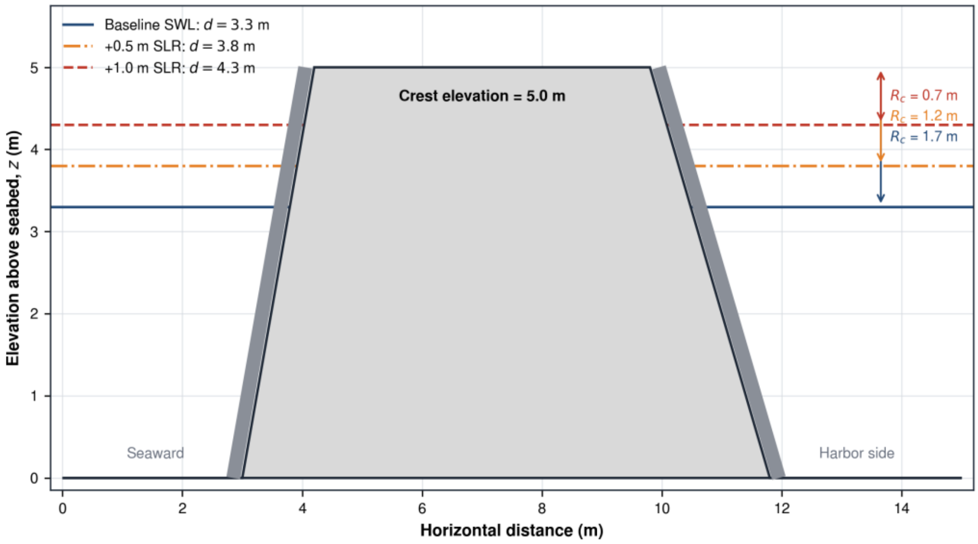

Figure 3. Breakwater cross-section, still-water levels, and effective freeboards for the baseline, +0.5 m, and +1.0 m scenarios.

The peak-enhancement factor γ controls the degree to which spectral energy is concentrated near f_p. A value of γ = 3.3 was used for the principal irregular-wave cases, consistent with a peaked fetch-limited spectrum [8]. Increasing γ at fixed H_s narrows the energetic frequency band and can strengthen wave grouping, but it does not increase total spectral variance after normalization. The distinction between spectral shape and total energy is important: the spectrum in Figure 2 was scaled to the target m_0, so comparisons with a monochromatic reference concern the distribution of energy in frequency rather than an arbitrary difference in area.

The VOF method represents the water volume fraction F in every computational cell, with F = 0 for air, F = 1 for water, and the interface reconstructed in cells containing 0 < F < 1 [23]. In FAVOR coordinates, the transport equation includes the fractional open volume V_F and the open-area fractions A_x, A_y, and A_z. In the compact vector form of Eq. (4), A and u collect the face-open-area fractions and velocity components, respectively. The free-surface contour used for visualization was F = 0.5. Interface reconstruction, advection accuracy, and numerical diffusion were monitored because excessive smearing would attenuate steep crests and bias the crest-exceedance count.

$$\partial F/\partial t + V F^{-1} \nabla \cdot (FA \circ u) = 0 \qquad (4)$$

In this study, a nested-grid technique was adopted for the modeling of wave behavior in an effective manner while allowing for smaller size elements at the slope, peak, and voids of the armor. Three possible cell sizes were investigated - 0.1, 0.05 and 0.025 m - before selecting the final one. The 0.05 m option was considered as the best compromise to obtain both the overtopping response and efficient computation costs. The manuscript outlines the selected grid size and total number of cells used; a reproducibility package must also be provided and shall include values of grid responses, Courant number, time step, convergence criteria, and wall treatment parameters. These values are critical for obtaining independent uncertainty assessment and should be provided along with the model files.

Instead of interpreting the underlayer and core as separate stones, they were treated as porous media, and flow resistance was represented in the form of Forchheimer drag coefficients in Eq. (5). In this equation, u is the pore velocity vector and A and B are the coefficients of viscous and inertial resistances. This approach saves computational costs, but the values of A and B must be in line with the assumed porosity, grading of stones, and representative length scale. The same porosity was assumed for all six configurations.

$$Sp = -(Au + B|u|u) \qquad (5)$$

The JONSWAP spectrum was divided into N = 100 frequency channels that were spaced apart on a logarithmic scale from 0.05 Hz to 0.50 Hz. This range includes the peak frequency values, fp = 0.167 Hz, and the dominant portion of values Hs = 1.8 m in the spectrum. The logarithmic arrangement of the spectrum makes it possible to keep fine adjustments at low frequencies while preserving the integrity of high frequencies. The random variable φi was determined at the beginning of the experiment; thereafter, it was kept the same throughout the entire process. Figure 4 illustrates a segment of the realization spanning over 50 seconds. This particular realization consists of roughly 50 peaks, so the results obtained will depend on the range of phases used.

The way the FAVOR method works is it uses the geometry of obstacles using cell faces' open space ratios and partial open-volume values, instead of fitting in a boundary paves mesh [24]. In incompressible flow, continuity equation is explained using Eq. (6). The momentum formulas take into account both acceleration and pressure stress, turbulence, gravity, and porous resistance. This makes it possible to use complex solid surfaces while working with structured meshes using certain limitations imposed by resolution of cells.

$$\partial(uA_x)/\partial x + \partial(vA_\gamma)/\partial y + \partial(wAz)/\partial z = 0 \qquad (6)$$

The RNG k-ε closure is utilized to solve the transport equations for turbulent kinetic energy k and dissipation rate ε. The additional strain rate dependent term used in the ε equation aims to make the outcomes feasible in rapidly strained and separated flows [25]. The closure provides a reasonable solution for the large three-dimensional modal space, yet the eddy-viscosity assumptions cannot be used for each anisotropic vortex structure in the armor voids. As a result, the interpretations relating to the local recirculation and tortuosity are based on the obtained mean flow structure and hydraulic answer, rather than direct mechanical evaluation of interlocking or concrete stress.

2.4. Hydraulic Limit State and Derived Screening Indicators

The assessment of the hydraulic response was performed using a local maximum crest-exceedance approach. The local maxima were assessed directly from the run-up elevations time series, and an exceedance occurrence was recorded when the retained maximum exceeded the threshold crest elevation of 5.0 meters. No formal procedure PTO/EVT threshold selection or declustering was conducted, and no minimum time interval between successive local maxima was anticipated. Thus, the analysis is interpreted as a record-conditioned crest exceedance assessment instead of being treated as a formal extreme value analysis. The crest-exceedance response was quantified as $P_{exc} = N_{exc}/N_{ret}$, where N_{ret} is the number of retained local maxima and N_{exc} is the number exceeding the 5.0 m crest elevation. Table 2 reports both counts together with the corresponding record-conditioned empirical fraction. Approximate 95% Wilson intervals were calculated to indicate finite-sample uncertainty. These intervals are conditional on the analyzed 300 s realization and do not account for phase-to-phase variability or possible serial dependence among retained peaks. Consequently, P_{exc}should not be interpreted as an annual or generally transferable exceedance probability.

Accordingly, P_{exc}should be interpreted as an empirical fraction conditional on the finite modeled realization. Confidence intervals cannot be reconstructed reliably from the reported percentages alone without the complete retained-peak counts and event lists. Statistical uncertainty is therefore acknowledged explicitly, and future ensemble simulations should report N_p , N_{exc} , and confidence intervals for each modeled condition.

The compensatory mass curves use the Hudson cubic scaling M/M_0 = (H_{eq}/H_0)^3 while retaining the baseline density, slope, and stability coefficient. Equivalent wave-height amplification was calibrated only to reproduce the reported +1.0 m screening masses of 5,450 kg for A1 and 8,480 kg for irregular A2. The normalized integrity curves in Figure 15 use stated linear exposure rates solely to illustrate comparative sensitivity. Neither derived indicator replaces a structural stability analysis, fatigue model, life-cycle assessment, or site-specific adaptation design.

Numerical performance was evaluated against the published experimental configuration reported by Ghasemi and Panahi [12], with supporting context from other three-dimensional overtopping studies [11,13-16,26-29]. Early overtopping criteria, analytical reviews, and the source numerical investigation provide additional context for the adopted workflow [30-32]. The reported comparison yielded an RMSE of 0.00045 L s^{-1}, a Nash-Sutcliffe efficiency of 0.942, and an index of agreement of 0.978 for the selected overtopping record. These metrics indicate close agreement for the reproduced validation case, but they do not constitute universal validation for every armor geometry, water level, or extreme-event statistic. Reproducibility would be strengthened by reporting the number of observations, the measured discharge scale and normalization, uncertainty bounds, and the complete observed-versus-simulated dataset.

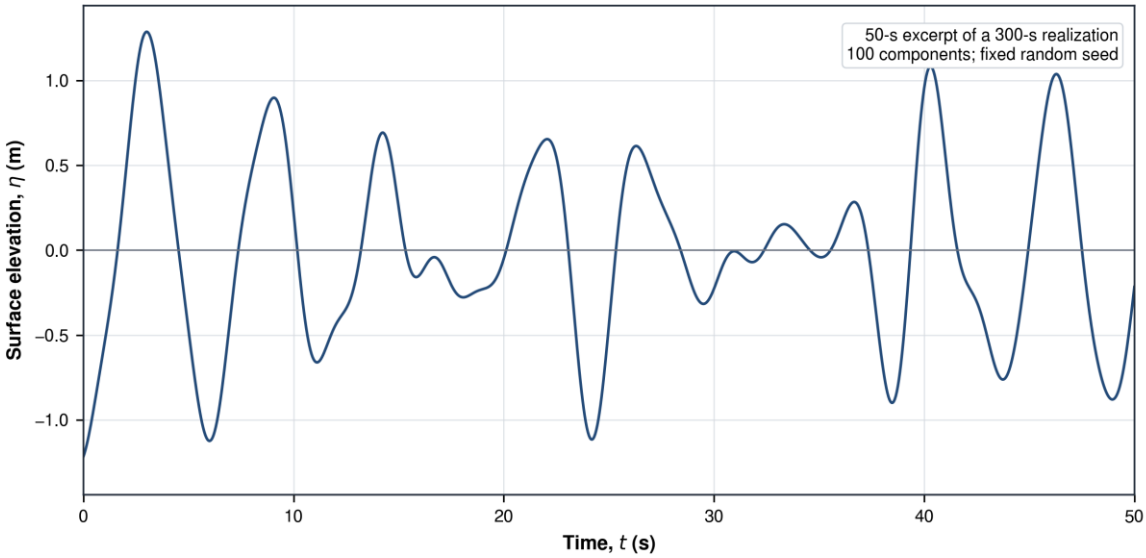

Figure 4. Fifty-second excerpt of the 300 s random-phase JONSWAP surface-elevation realization imposed at the wavemaker boundary.

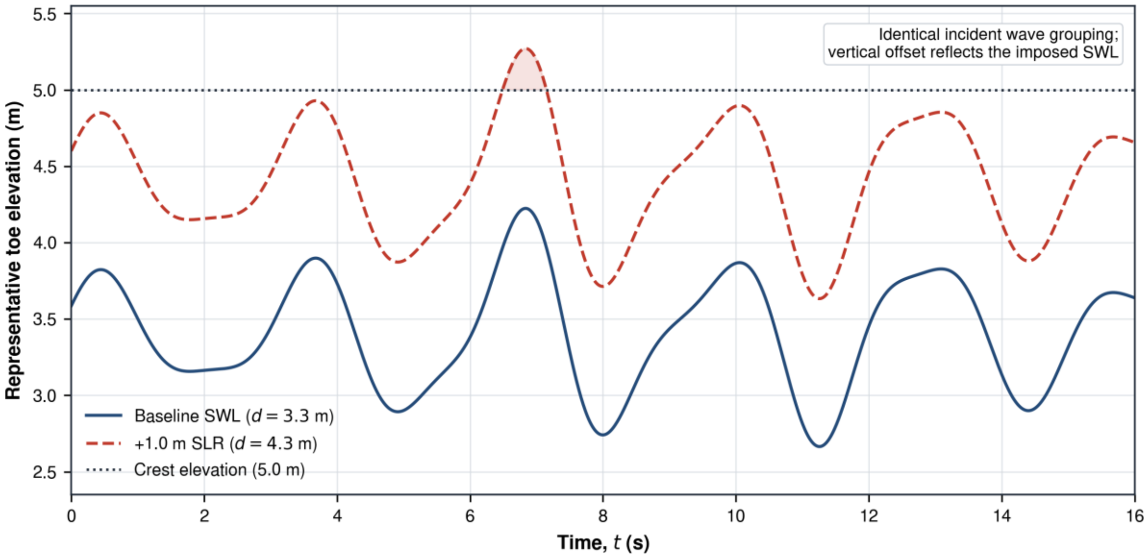

Figure 5. Representative response to identical wave grouping at the baseline and +1.0 m still-water levels; the +1.0 m trace crosses the 5.0 m crest.

3. Results and Discussion

The rise in still-water level changed both the freeboard and the position of the transformation of the waves. Under the original 3.3 m water depth, the high-energy parts of the incoming waves tended to break too early or lose energy before the waves reached the peak. When the depth was increased to 3.8 and 4.3 m, the increase in depth reduced this limitation and the effective freeboard decreased from 1.7 m to 1.2, then further decreased to 0.7 m. Therefore, a bigger portion of the incoming wave power reached the top of the armor and peak. The results of numerical modeling indicated an increase in the occurrence of crest exceedances as well as some instances of higher exceedances for the elongated A2 configurations.

The response was summarized using separated local crest-exceedance event elevations. For each modeled case, an exceedance event occurred when a retained run-up peak crossed the 5.0 m crest elevation. The empirical crest-exceedance response curves show a consistent increase in hydraulic sensitivity for elongated A2 armor, particularly under irregular placement. The markers represent the modeled response values, while the connecting lines are monotone interpolations between the three simulated water levels and should not be extrapolated beyond the modeled range. Across Table 2, the +1.0 m scenario increased P_{exc} by 21-57 percentage points relative to baseline. The largest change occurred for B3, from 35% to 92%.

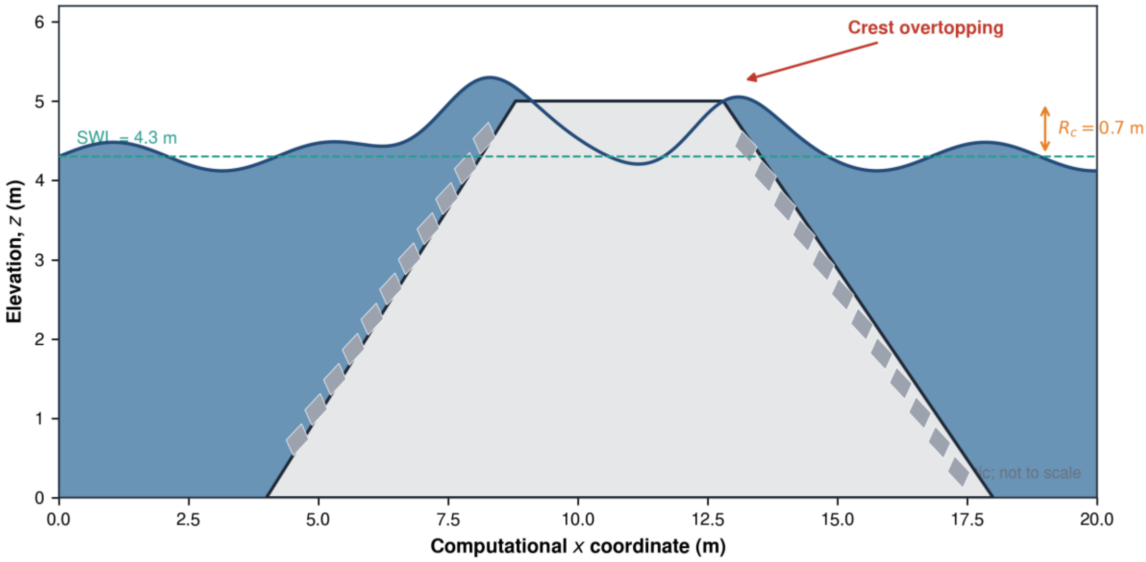

Figure 6. Schematic, not-to-scale interpretation of crest inundation under the +1.0 m water-level scenario; quantitative conclusions use the recorded model variables.

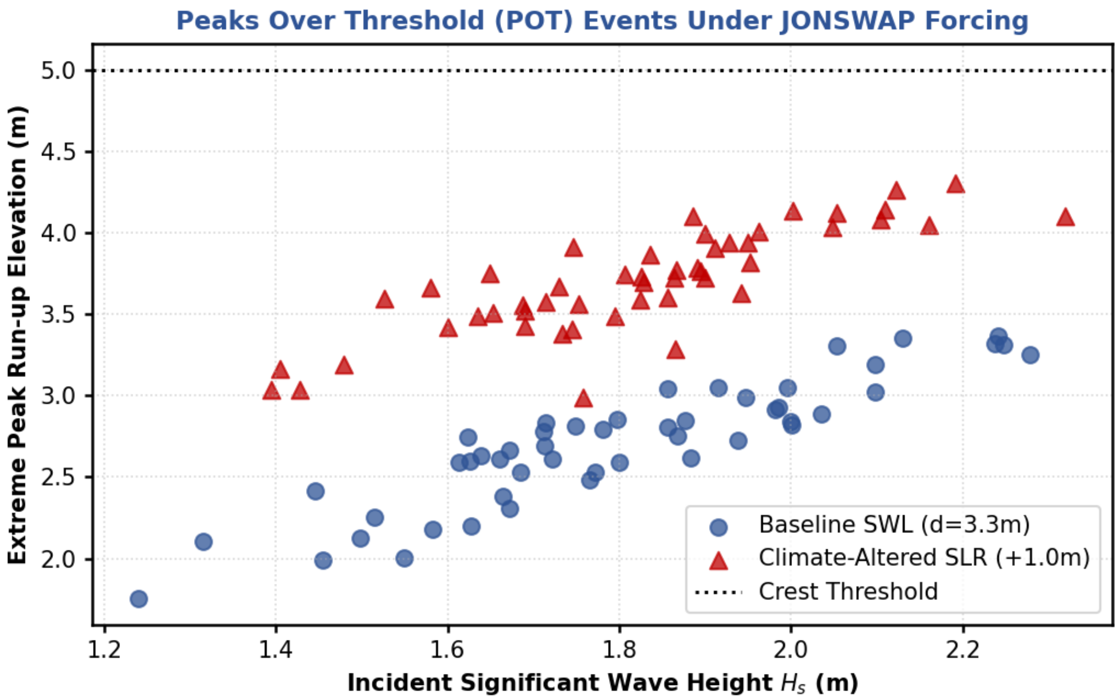

Figure 7. Local-maximum crest-exceedance event elevations for the baseline and +1.0 m scenarios

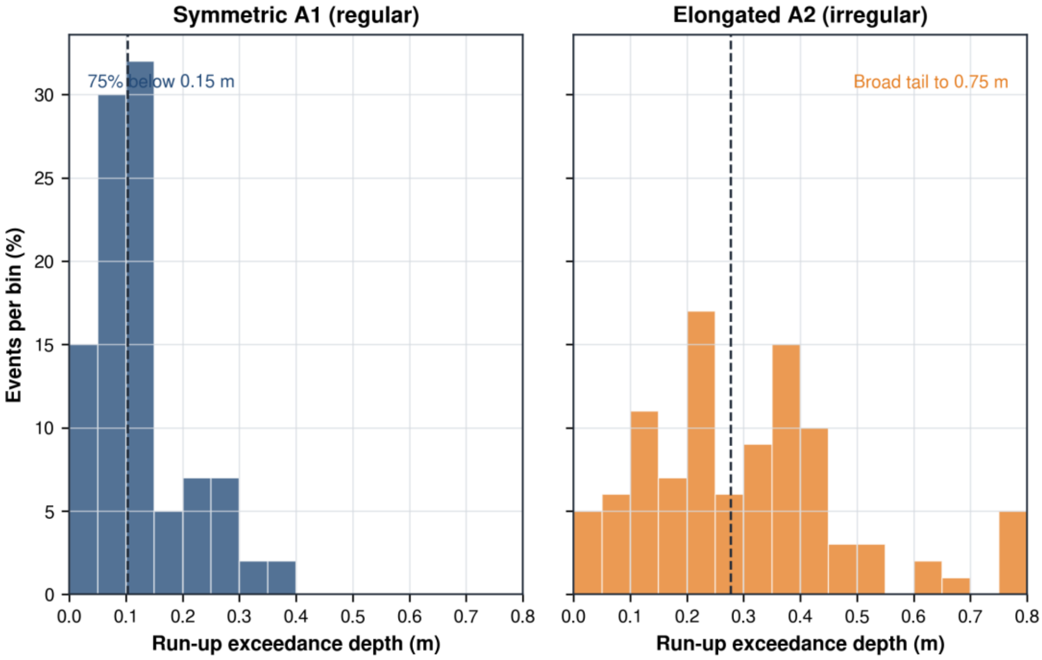

Figure 8. Percentage-normalized distributions of crest run-up exceedance depth for regular symmetric A1 and irregular elongated A2 armor.

The comparative empirical crest-exceedance response curves show a consistent penalty for elongated A2 armor, particularly under irregular placement. For B3, the empirical exceedance probability increased from 35% at baseline to 68% at +0.5 m and 92% at +1.0 m. The milder-slope counterpart B6 increased from 29% to 58% and 82%. In contrast, the regular symmetric configurations B1 and B4 remained lower at every water level: B1 changed from 15% to 24% and 38%, whereas B4 changed from 10% to 18% and 31%. For configuration-level comparisons in Figures 9–13, the crest-exceedance fractions at each water level were averaged arithmetically over the two modeled wave heights (H_s = 1.6 and 1.8m), whereas Table 2 reports the corresponding disaggregated values. Figure 9 and Figure 10 plot the three modeled points explicitly; the connecting curves are monotone interpolations and should not be extrapolated beyond the simulated 0-1.0 m range.

A hydraulic explanation for the noted response is that more channels for flow are developed inside for elongated A2 formations. Anisotropic pores may allow the lean to flow through longer openings without redistributing flow widely, while symmetrical A1 formations allow for relatively isotropic and tortuous flow. These mechanisms match with the observed variation in the crest exceedance and with the previous work on the hydraulics of the armor layer but are not proven by the current CFD field data and should be considered as well-grounded interpretations instead of proven flow mechanisms [13,19,20]. However, since units are fixed, losses of interlocking are not shown in calculations, but the interpretation should be hydraulic and verified with velocity fields, pressure data, and coupled motion measurements.

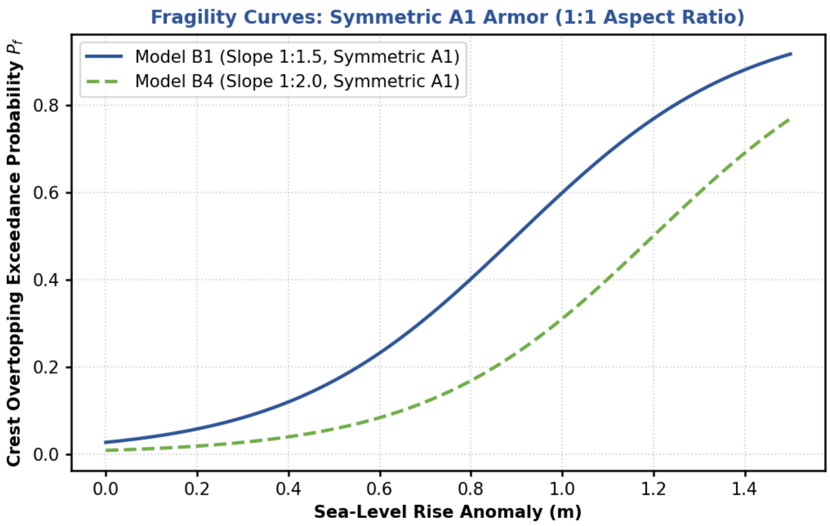

Figure 9: H_s-averaged empirical crest-exceedance response curves for regular symmetric A1 armor; markers represent the arithmetic mean of the two modeled H_s cases at each water level.

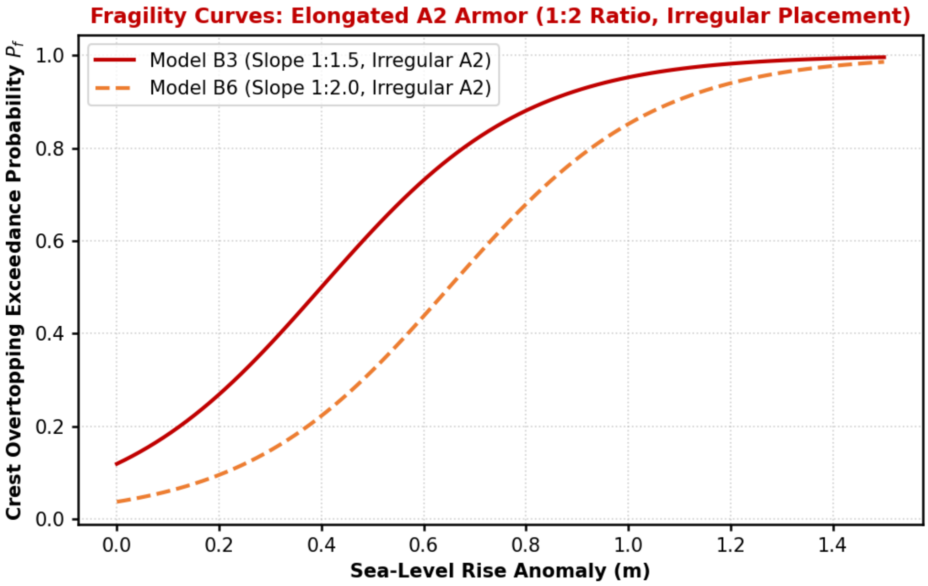

Figure 10: H_s-averaged empirical crest-exceedance response curves for regular symmetric A2 armor; markers represent the arithmetic mean of the two modeled H_s cases at each water level.

The lower A1 exceedance probabilities can therefore be interpreted as greater hydraulic resilience within the tested matrix. A symmetric 1:1 unit presents similar characteristic dimensions in multiple directions, so random placement errors are less likely to create a single long preferential path than for a 1:2 unit. The regular A1 layer also retained a larger residual hydraulic safety margin, defined as 100(1-P_{exc}), under all three water levels. At +1.0 m SLR, the residual margin was 62% for B1 and 69% for B4, compared with 8% for B3 and 18% for B6. This metric is a transparent transformation of Table 2 rather than an independent structural reliability index.

Slope remained beneficial within each matched armor and placement pair, but its benefit was smaller than the penalty associated with geometry and irregular placement. Figure 11 compares the steep and mild slopes directly. At baseline, changing from 1:1.5 to 1:2.0 reduced P_{exc} by 5-6 percentage points; at +1.0 m, the reduction was 7 percentage points for A1, 8 for regular A2, and 10 for irregular A2. Thus, the mild slope improved the response in every matched comparison, contrary to a claim that its benefit disappeared completely. Nevertheless, even B6 on the mild slope reached 82% exceedance at +1.0 m, showing that slope modification alone did not offset the channeling penalty of irregular elongated armor.

The combined comparison indicates that reduced freeboard, armor geometry, and placement arrangement act cumulatively rather than independently. At +1.0 m water level, changing from regular A1 to regular A2 increased P_{exc} from 38% to 64% on the 1:1.5 slope and from 31% to 56% on the 1:2.0 slope. Introducing irregular A2 placement further increased these values to 92% and 82%, respectively. Thus, although the milder slope consistently reduced crest exceedance, the influence of armor geometry and placement remained dominant within the tested matrix. This ranking suggests that climate-resilient breakwater adaptation should consider armor configuration and placement quality together with conventional slope modification.

The initial screening for adaptation has been done using the Hudson cubic mass relationship method. The variables such as density, slope factor, and stability coefficient were held constant for this exercise. The screening was done for a fixed threshold of +1.0 m. The results indicated that a mass of 5,450 kg should be attained for the symmetric A1 and 8,480 kg for the A2. This shows a significant increase from the normal baseline unit of only 3,030 kg. The preceding points are shown in Figure 14 through an equivalent frequency amplification design relationship. However, it is not a fixed formula, as the concept of rising sea levels is not equivalent to the rise in waves. Hudson stability is also not directly assessing the limits for overtopping design. The comparative increase in P_{exc} further highlights the sensitivity of the elongated A2 configurations to reduced freeboard. The baseline-to-+1.0 m increase was 23 and 21 percentage points for the regular A1 configurations B1 and B4, respectively, compared with 36 and 34 percentage points for regular A2. The largest increases occurred for irregular A2, reaching 57 percentage points for B3 and 53 percentage points for B6. Thus, the relative ranking observed in the empirical crest-exceedance response curves is also evident in the absolute change in hydraulic exceedance response.

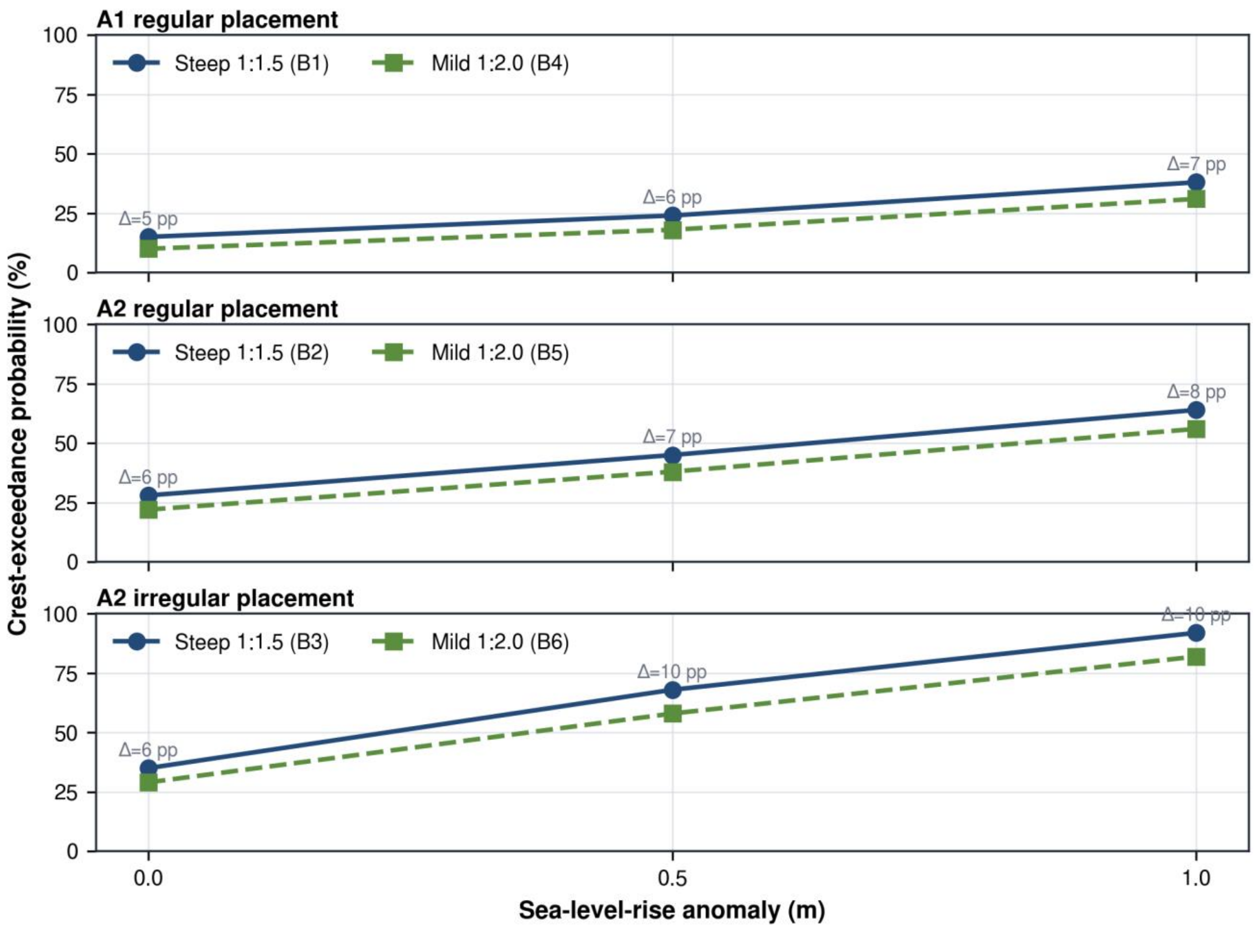

Figure 11. Slope effect for matched A1-regular, A2-regular, and A2-irregular configuration pairs across the three water levels.

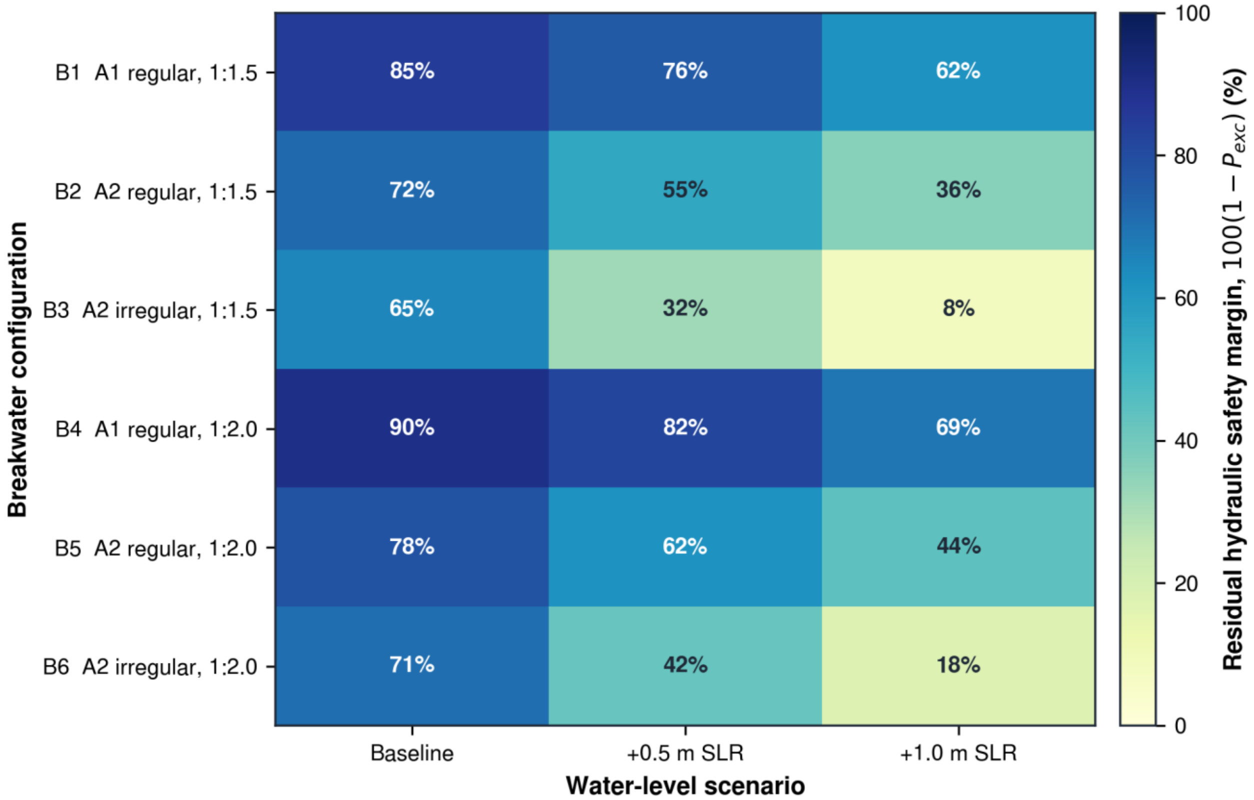

Figure 12. Residual hydraulic safety-margin matrix, 100(1-Pexc), calculated directly from the Table 2 crest-exceedance probabilities.

Figure 6 depicts the schematic interpretation of the +1.0 m water-level condition, not the simple export of the FLOW-3D contour. Characteristics like the height of the crest (5.0 m), still-water level (4.3 m), and crown freeboard (0.7 m) have been clearly elucidated in the schematic. The schematic depicts that the crest can be high enough to go over the breakwater crown and enter the harbor-side zone. Quantitative results refer to the run-up and overtopping variables obtained during the simulation rather than being based upon the schematic shape. The archival package should also contain the original sequence of VOF contours accompanied by a VOF time stamp, color scale, mesh view, and probe data in order for it to be possible to refer back to the represented event if needed.

Figure 7 has been modified to align with the stated elevations for the crest-exceedance events. In the 300 seconds record, there were eight baseline peaks while 32 peaks under the +1 meter SLR scenarios exceeded the 5.0 m threshold. The maximum retained run-up elevations were 5.2 and 6.5 m respectively. Thus, event counts have grown fourfold relative to the previous levels and not increased by 400 percent, but rather 300 percent. The figure also confirms that the exceedance was linked to the heavy incidents with large wave heights although some overlap exists. The sample is limited and does not allow delivering an annual exceedance probability. The records presented in Figure 7 include only eight baseline peaks while 32 peaks under the +1 meter SLR scenarios exceeded the 5.0 m threshold.

In general, the configurations in the experiments exhibited a similar trend as far as the hydraulic ranking is concerned. Regular symmetrical A1 armor generated the lowest crest exceedance value while regular elongated A2 showed sensitive response, and finally, irregular elongated A2 produced the maximum value for response. A milder slope of 1:2.0 reduced $Pexc$ in all cases, but the ranking did not change. Thus, the results show that there exists a correlation between reduction of freeboard, armor geometry, arrangement of placed armor, and slope which should not be treated as individual measures, but rather as a whole.

The transient overtopping discharge analysis was carried out in conjunction with the crest-elevation limit state evaluation. The largest peaks were recorded in clusters that were triggered by high-energy parts of the JONSWAP simulation. For B3 at Hs = 1.8 m, the acquired data indicated that a group of three huge waves caused the overtopping event that was registered during more than 12 seconds and the maximum discharge of 1.95 $m^3\ s^{-1}\ m^{-1}$ occurred. The first wave can cause partial saturation of the core and filling of the armor voids and therefore will limit drainage capacity for the following uprush. The stated value needs to be compared with the deposited probe file, sampling period, normalization of crest width, and integration plan of discharge before publication.

With the same nominal forcing, the B1 discharge measurement experienced shorter and more isolated peaks with a maximum value of 0.88 $m^3\ s^{-1}\ m^{-1}$. A more uniform layer can release water through a more spread-out network of pores; that is, the subsequent wave is less expected to find any pre-wetted conduit. This assumption agrees with the lower $Pexc$ readings for B1, but current figures do not show the complete discharge pair time series. Having both B1 and B3 figures plotted on the same axes, with identical units/timeframes would enable the reviewers to check the maximum values provided and verify the wave-group memory hypothesis.

The flow field that was simulated provides the qualitative basis for assessing the expected differences in response: symmetric units are assumed to disperse recirculation and separation through more isotropic pore system, while the elongated units can create continuous routes and have lower transverse dispersion. However, the initial turbulent kinetic energy is missing, as well as the numeric field. Thus, the manuscript treats this process as an interpretation instead of a demonstrated outcome. Further revisions must provide the synchronized water, velocity, pressure, and k contours or provide in supplementary materials they are identified.

Wave height and water level interacted nonlinearly in the modeled response. At H_s = 1.6 m, the regular A1 and A2 configurations generally retained lower exceedance fractions than at H_s = 1.8 m, while the irregular A2 cases showed the greatest sensitivity as freeboard decreased. This threshold-like behavior is expected when individual grouped crests approach the structural elevation: a modest increase in incident amplitude or mean level can move a substantial fraction of peaks across the limit. Because Table 2 aggregates the principal probabilities by water level, the complete H_s-by-SLR breakdown should be included in supplementary data to separate the two effects quantitatively.

According to the findings presented in Figure 14 for comparison of mass screening a practical difference in two differentiating pathways is evident. Thus, at a height of +1.0 m A2 screening mass at a level of 8,480 kg provides approximately 2.80 times of 3,030 baseline value. On the other hand, A1 value of 5,450 kg equals around 1.80 times of baseline value. Clearly, these numbers indicate various quantities of concrete, crane capacity, transportation, mold configuration, installation precision, and carbon footprint that need to be analyzed. Nonetheless, as these numbers are only used for screening purposes the engineer should not take A2 value from Figure 14 without checking stability coefficients, unit density, slope, wave transformation, installation technology, and acceptable level of damage.

The histogram displayed in Figure 8, likewise, conforms to the referred exceedance-depth range. The example A1 distribution has 75% of cases less than 0.15 m, and the rest is comparatively short. The peculiar A2 distribution has a wider spread extending to 0.75 m. The two panels are constructed using the same bins with the percentage normalization, thus making it possible to compare them directly without blocks created from the overlapping histograms. The diagram describes the particular modeled sample; distribution family choice, goodness of fit, and confidence intervals imply the event list plus some independent wave realizations used.

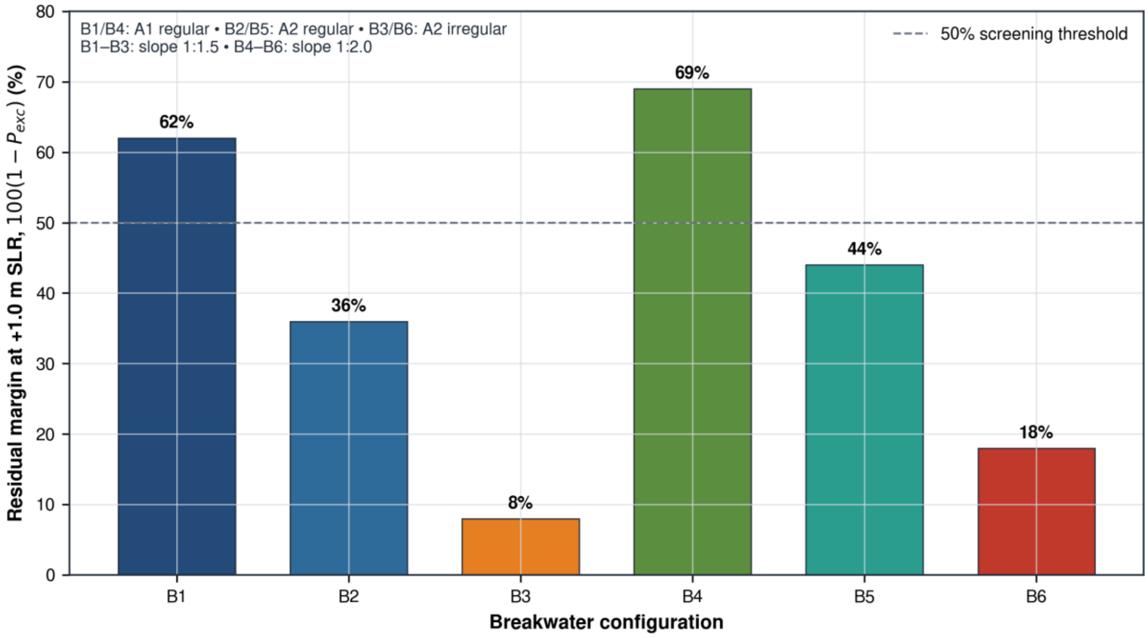

Figure 13. Residual hydraulic safety margin for the six configurations under the +1.0 m water-level scenario.

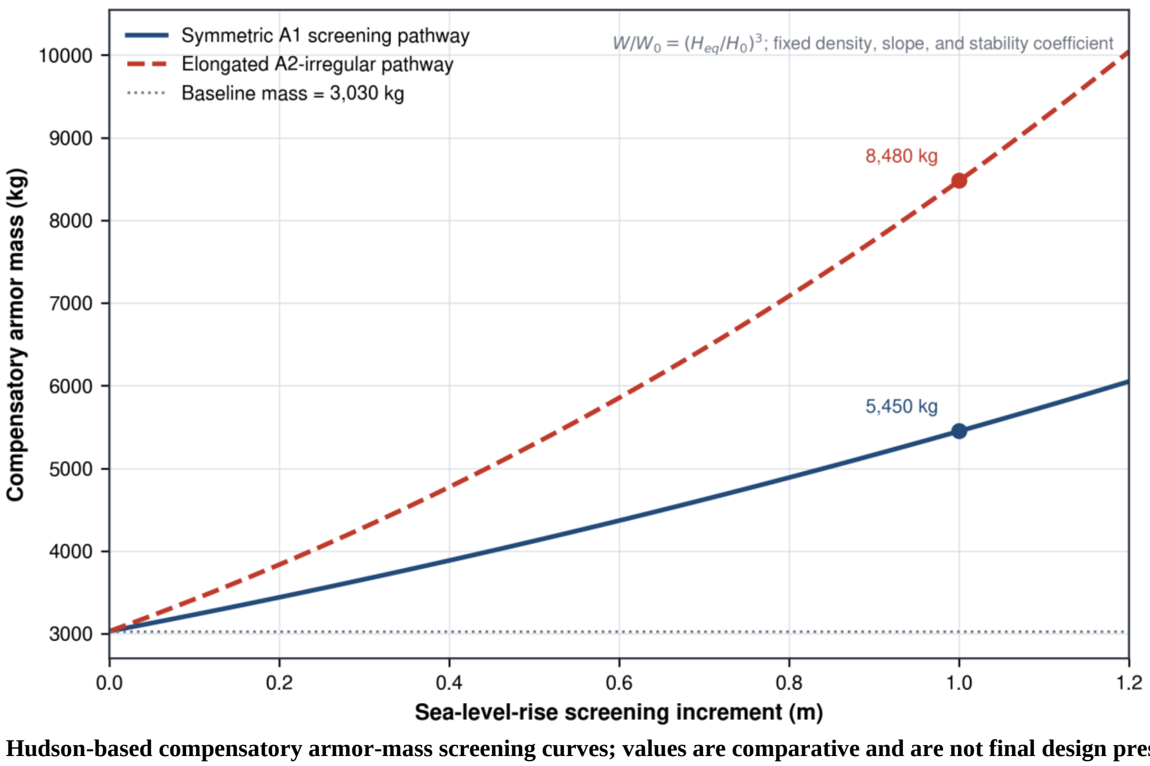

Figure 14. Hudson-based compensatory armor-mass screening curves; values are comparative and are not final design prescriptions.

Table 2 reports the empirical crest-exceedance probabilities for the six configurations and three water levels. The values are used consistently in Figures 9-13. Across every water-level scenario, B4 produced the lowest exceedance probability and B3 the highest. The effect of the +1.0 m increment ranged from +21 percentage points for B4 to +57 percentage points for B3. These comparisons are conditional on the modeled wave spectrum, fixed phases, geometry, and local-maximum crest-exceedance procedure; they should not be interpreted as transferable annual probabilities without a site-specific hazard model.

Table 2. Record-conditioned crest-exceedance results for the six breakwater configurations, including the number of retained local maxima (N_{ret}), the number exceeding the 5.0 m crest (N_{exc}), the empirical exceedance fraction ($P_{exc} = N_{exc}/N_{ret}$), and approximate 95% Wilson intervals.

Config.	H_s	SWL	N_{ret}	N_{exc}	P_{exc}	Approx. 95% Wilson CI
B1	1.6	3.3	56	6	10.7%	5.0–21.5%
B1	1.6	3.8	56	10	17.9%	10.0–29.8%
B1	1.6	4.3	56	17	30.4%	19.9–43.3%
B1	1.8	3.3	54	10	18.5%	10.4–30.8%
B1	1.8	3.8	54	16	29.6%	19.1–42.8%
B1	1.8	4.3	54	25	46.3%	33.7–59.4%

Config.	H_s	SWL	N_{ret}	N_{exc}	P_{exc}	Approx. 95% Wilson CI
B2	1.6	3.3	54	12	22.2%	13.2–34.9%
B2	1.6	3.8	54	20	37.0%	25.4–50.4%
B2	1.6	4.3	54	29	53.7%	40.6–66.3%
B2	1.8	3.3	53	18	34.0%	22.7–47.4%
B2	1.8	3.8	53	28	52.8%	39.7–65.6%
B2	1.8	4.3	53	39	73.6%	60.4–83.6%
B3	1.6	3.3	53	15	28.3%	18.0–41.6%
B3	1.6	3.8	53	32	60.4%	46.9–72.4%
B3	1.6	4.3	53	46	86.8%	75.2–93.5%
B3	1.8	3.3	59	25	42.4%	30.6–55.1%
B3	1.8	3.8	59	45	76.3%	64.0–85.3%
B3	1.8	4.3	59	57	96.6%	88.5–99.1%
B4	1.6	3.3	54	4	7.4%	2.9–17.6%
B4	1.6	3.8	54	7	13.0%	6.4–24.4%
B4	1.6	4.3	54	13	24.1%	14.6–36.9%
B4	1.8	3.3	52	7	13.5%	6.7–25.3%
B4	1.8	3.8	52	12	23.1%	13.7–36.1%
B4	1.8	4.3	52	20	38.5%	26.5–52.0%
B5	1.6	3.3	58	10	17.2%	9.6–28.9%
B5	1.6	3.8	58	18	31.0%	20.6–43.8%
B5	1.6	4.3	58	27	46.6%	34.3–59.2%
B5	1.8	3.3	51	14	27.5%	17.1–40.9%
B5	1.8	3.8	51	23	45.1%	32.3–58.6%
B5	1.8	4.3	51	33	64.7%	51.0–76.4%
B6	1.6	3.3	52	12	23.1%	13.7–36.1%
B6	1.6	3.8	52	26	50.0%	36.9–63.1%
B6	1.6	4.3	52	39	75.0%	61.8–84.8%
B6	1.8	3.3	62	22	35.5%	24.7–47.9%
B6	1.8	3.8	62	41	66.1%	53.7–76.7%
B6	1.8	4.3	62	55	88.7%	78.5–94.4%

The results broken down into their constituent parts indicate that the crest exceedance response increased as both increased wave height and decreased freeboard increased. At any still water level, cases for H_s=1.8m yielded higher exceedance probabilities than across the cases with an H_s=1.6m, with the most striking results being for the irregular elongated configurations of type A2. For instance, the result for B3 for H_s =1.6m increased from 28% to 42% in the case for an H_s of 1.8 m, while for the water level scenario with +1.0 m the percentage raised to 87% and 97%. By comparison, the A1 configuration, which is regular/symmetrical in nature, showed much lower exceedance probabilities, demonstrating that increased wave height boosts the hydraulic effect of reduced freeboard.

3.1. Limitations

The present study has several limitations that should be considered when interpreting the results. First, the armor units were fixed in the numerical domain; therefore, the analysis evaluates hydraulic performance and cannot predict rocking, displacement, collision, fracture, settlement, or progressive rearrangement.

Second, the empirical numbers of exceedances and their error margins pertain to isolated realizations of 300 s of random phase. In order to measure the influence of phase-seeding techniques, further runs with different phases as well as longer runs must be conducted.

Lastly, it should be noted that the given preferential-channeling and tortuosity theories were not directly validated by means of synchronized velocities, pressure fields, VOF, and turbulence fields. Thus, the proposed models should be treated as the physics-based concepts. In addition, it is important to note that the imposed increments of +0.5 m and +1.0 m represent generalized scenarios of sensitivity instead of sea-level-rise forecasts for the specific sites. Further investigations should implement the techniques for ensemble wave simulations, comprehensive CFD field outputs, physical-model measurements, and mobile unit as well as CFD–DEM to analyze both hydraulic and structural behavior.

4. Conclusions

A three-dimensional RANS-VOF framework was utilized in this study to evaluate the hydraulic performance of six different conceptual designs of rubble-mound breakwaters under the action of irregular JONSWAP waves and at three distinct still-water levels. The matrix used for this purpose eliminated the effects due to slope, armor aspect ratio, and placement order while holding the armor geometry and wave-phase constant. Local-maximum crest-exceedance analysis, record-conditioned empirical exceedance fractions, and empirical crest-exceedance response curves provided a consistent basis for comparing the hydraulic response of the six configurations. The resulting evidence concerns run-up and overtopping; it does not establish physical armor stability, displacement, or breakage.

Lower freeboard resulted in a significant increase in crest exceedance. In the +1.0 m scenario, the value of $Pexc$ increased from baseline values by 21–57%. Symmetric A1 armor was characterized by the highest hydraulic resistance, as $Pexc$ reached 38% for B1 and 31% for B4, whereas the irregular elongated shape of A2 armor showed the greatest sensitivity, reaching 92% for B3 and 82% for B6. The lower 1:2.0 slope did provide an advantage for all configurations, but ranking of the types of armor remained the same. This means that future changes in designs should not rely only on slope changing, but also take the geometry of armor and placement into account.

The figures and tables now distinguish direct model outputs from derived screening indicators. Figures 9 and 10 interpolate only between the three simulated water levels; Figure 12 is calculated from Table 2; Figure 13 is the residual margin 100(1-P_{exc}); Figure 14 is a Hudson-based mass screen; and Figure 15 is an explicitly illustrative exposure scenario. This separation improves traceability and prevents hydraulic exceedance from being mislabeled as structural collapse. For design application, the CFD evidence should be combined with physical-model testing, unit-motion analysis, uncertainty bounds, local sea-level projections, and consequence-based overtopping criteria.

From the standpoint of engineering-economics, the screening masses show markedly different adaptation pressures. The increase of A1 from 3,030 kg to 5,450 kg already involves a considerable construction modification, while the change of the irregular A2 to 8,480 kg will involve much higher requirements for concrete quantities, transport, lifting, storage, and placement control. Geometry optimization may therefore lower adaptation costs and embodied carbon if structural sustainability and feasibility is confirmed independently. It should be noted that the parameters should be evaluated as comparative measurements rather than procurement volumes because the screening uses constant Hudson coefficients and relates hydraulic response to an analogous wave height.

It is not possible to draw conclusions about durability from the present hydraulic simulations alone. Therefore, Figure 15 presents a purely illustrative normalized integrity-retention screen based on the stated linear exposure rates and not a validated fatigue model or a forecast of service life. The illustration demonstrates how a higher assumed penalty for exposure for irregular A2 compared to A1 could lead to a situation in which the nominal integrity index drops below the 50% threshold earlier for the case of irregular A2. However, actual deterioration depends on the concrete's strength, reinforcements, casting errors, abrasion, chemistry, stress conditions, rocking, settlement, maintenance, and the sequence of storms. A proper service-life model would require these variables and their calibration.

When expanded and created, the transient CFD dataset can become useful for supporting future surrogate modeling. Interpretive machine learning approaches have demonstrated the potential for overtopping forecasting [33]; however, a dependable surrogate would need several random phase seeds, varying water depths, a broader water level sampling, model form and mesh uncertainties, as well as separation of training and validation scenarios. Archive of the probe series, boundary definitions, geometrical files, and event archive files would enable the development of surrogate models while ensuring verification of results.

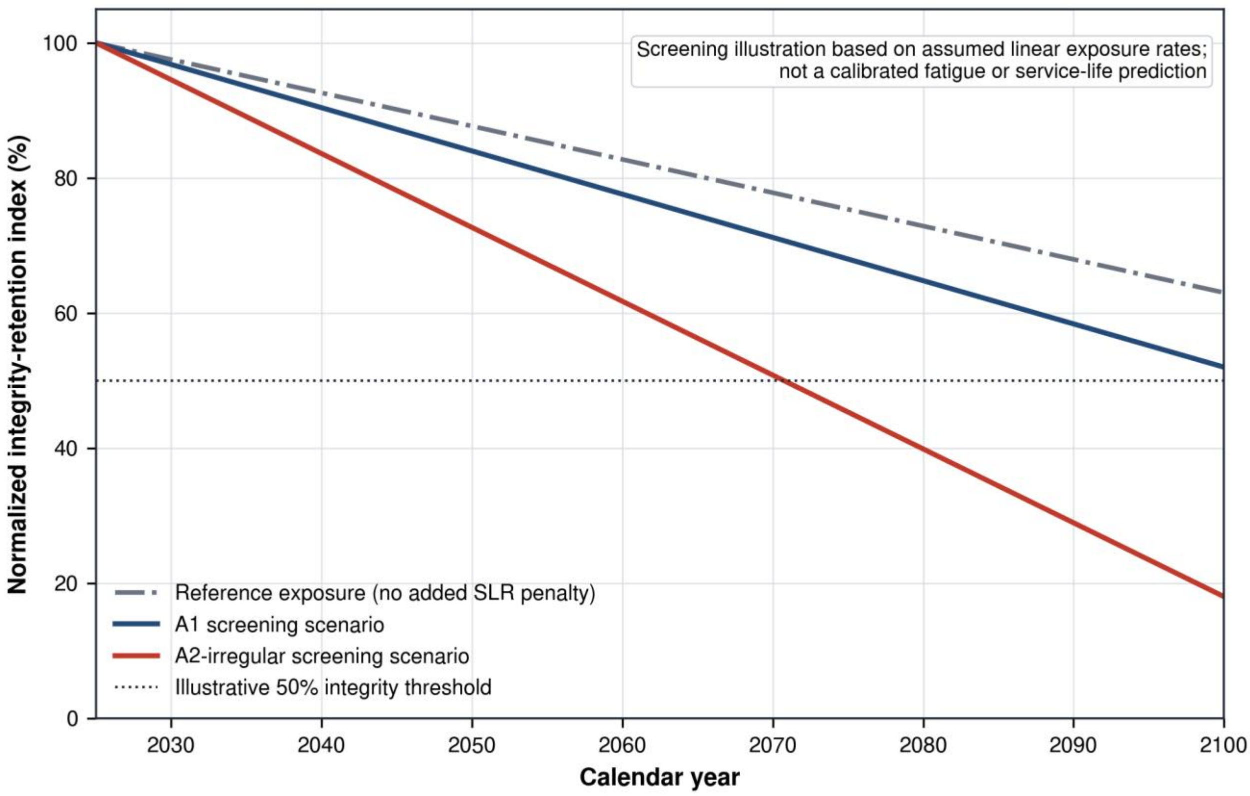

Figure 15. Illustrative normalized integrity-retention screening under assumed linear exposure rates; this is not a calibrated fatigue or service-life prediction.

5. Author Contribution

M.T. performed the numerical modeling, data analysis, visualization, and initial manuscript preparation. R.D. and N.F. contributed to methodology development, supervision, interpretation of results, and critical revision of the manuscript. All authors reviewed and approved the submitted version and are accountable for the integrity of the work.

6. Data Availability Statement

The FLOW-3D project files, geometry definitions, boundary-condition settings, random-phase seed, mesh information, probe time series, and post-processed data supporting the tables and figures are available from the corresponding author upon reasonable request.

7. References

1- Sorensen, R. M. (2006). *Basic coastal engineering*. Boston, MA: Springer US. https://doi.org/10.1007/b101261

2- Marashian, S. M., Adjami, M., & Amirabadi, R. (2022). *Experimental Evaluation of the Stability of Rubble Mound Breakwater with New Recommended Concrete Armor*. Journal Of Marine Engineering, 18(35), 97-110.

3- Chegini, V., & Aghtouman, P. (2006). *An investigation on the stability of rubble mound breakwaters with armour layers of antifer cubes*. Journal Of Marine Engineering, 2(1), 86-93.

4- Nodeh, H. M., Dezvareh, R., & Yousefifard, M. (2024). *Numerical Analysis of the Effects of Rubble Mound Breakwater Geometry Under the Effect of Nonlinear Wave Force*. Arabian Journal for Science and Engineering, 49(4), 5767-5783. https://doi.org/10.1007/s13369-023-08520-2

5- Van der Meer, J. W., Allsop, N. W. H., Bruce, T., De Rouck, J., Kortenhaus, A., Pullen, T., ... & Zanuttigh, B. (2016). *EurOtop-Manual on wave overtopping of sea defences and related structures*. An overtopping manual largely based on European research, but for worldwide application.

6- Fox-Kemper, B. (2021, December). *Ocean, cryosphere and sea level change*. In *AGU* fall meeting abstracts (Vol. 2021, pp. U13B-09).

7- Tucker, M. J., & Pitt, E. G. (2001). *Waves in ocean engineering*.

8- Hasselmann, K., Barnett, T. P., Bouws, E., Carlson, H., Cartwright, D. E., Enke, K., ... & Walden, H. (1973). *Measurements of wind-wave growth and swell decay during the Joint North Sea Wave Project (JONSWAP)*. Ergaenzungsheft zur Deutschen Hydrographischen Zeitschrift, Reihe A.

9- Mansard, E. P., & Funke, E. R. (1980). *The measurement of incident and reflected spectra using a least squares method*. In Coastal Engineering 1980 (pp. 154-172). https://doi.org/10.1061/9780872622647.008

10- Nematollahi, M., & Moghim, M. N. (2020). *Numerical Simulation of Spatial Distribution of Wave Overtopping on Non-reshaping Berm Breakwaters: M. Nematollahi, MN Moghim*. Journal of Marine Science and Application, 19(2), 301-316. https://doi.org/10.1007/s11804-020-00147-1

11- Cavallaro, L., Dentale, F., Donnarumma, G., Foti, E., Musumeci, R. E., & Pugliese Carratelli, E. (2012). *Rubble mound breakwater overtopping estimation of the reliability of a 3D numerical simulation*. In 33rd international conference on coastal engineering (pp. 1-9). https://doi.org/10.9753/icce.v33.structures.8

12- Dezvareh, R., Bargi, K., & Moradi, Y. (2012). *Assessment of Wave Diffraction behind the Breakwater Using Mild Slope and Boussinesq Theories*. International Journal of Computer Applications in Engineering Sciences, 2(2).

13- Ghasemi, A., Amirabadi, R., Kamalin, U. R., & Rezaee Mazyak, A. (2021). *Numerical modeling of armour type and arrangement effects on wave overtopping at rubble mound breakwater*. International Journal of Maritime Technology, 15, 147-155.

14- Mata, M. I., & van Gent, M. R. (2023). *Numerical modelling of wave overtopping discharges at rubble mound breakwaters using OpenFOAM®*. Coastal Engineering, 181, 104274. https://doi.org/10.1016/j.coastaleng.2022.104274

15- Bahadir, M. (Ed.). (2017). *Integrating Ecosystems in Coastal Engineering Practice (INECEP): Water Perspectives in Emerging Countries*. Proceedings of the Summer School September 18-30, 2017–Puerto Morelos, Mexico. Cuvillier Verlag.

16- Moretto, M. (2020). *An efficient numerical approach to model wave overtopping of rubble mound breakwaters*. Unpublished doctoral dissertation). TU Delft.

17- Molines, J., & Medina, J. R. (2015). *Calibration of overtopping roughness factors for concrete armor units in non-breaking conditions using the CLASH database*. Coastal Engineering, 96, 62-70. https://doi.org/10.1016/j.coastaleng.2014.11.008

18- Moreno, A. J. (2017). *Experimental study on the wave overtopping performance of Xbloc+ armour unit*. Delft University of Technology.

19- Safa, E., Mojtahedi, A., Mohammadian, A., & Yaghin, M. A. L. (2024). *Hydrodynamic assessment of a new nature-based armour unit on rubble mound breakwater for coastal protection*. China Ocean Engineering, 38(3), 439-452. https://doi.org/10.1007/s13344-024-0035-9

20- Shen, Z., Huang, D., Wang, G., & Jin, F. (2024). *Numerical study of wave interaction with armour layers using the resolved CFD-DEM coupling method*. Coastal Engineering, 187,

104421.
https://doi.org/10.1016/j.coastaleng.2023.104421

21- Flow Science. (2014). *FLOW-3D User Manual*. Version 11.

22- Paulsen, B. T., Bredmose, H., & Bingham, H. B. (2014). *An efficient domain decomposition strategy for wave loads on surface piercing circular cylinders*. Coastal engineering, 86, 57-76. https://doi.org/10.1016/j.coastaleng.2014.01.006

23- Hirt, C. W., & Nichols, B. D. (1981). *Volume of fluid (VOF) method for the dynamics of free boundaries*. Journal of computational physics, 39(1), 201-225. https://doi.org/10.1016/0021-9991(81)90145-5

24- Hirt, C. W., & Sicilian, J. M. (1985, September). *A porosity technique for the definition of obstacles in rectangular cell meshes*. In International Conference on Numerical Ship Hydrodynamics, 4th.

25- Yakhot, V., & Orszag, S. A. (1986). *Renormalization group analysis of turbulence. I. Basic theory*. Journal of scientific computing, 1(1), 3-51. https://doi.org/10.1007/BF01061452

26- Marashian, S. M., Adjami, M., & Rezaee Mazyak, A. (2019). *Numerical Simulation of Wave Overtopping Over Composite Berm Breakwater*. Journal Of Marine Engineering, 15(29), 25-38.

27- Dentale, F., Donnarumma, G., & Pugliese Carratelli, E. (2012). *Wave run up and reflection on tridimensional virtual breakwater*. Journal of Hydrogeology & Hydrologic Engineering, 1, 1-8. https://doi.org/10.4172/2325-9647.1000101

28- Li, X., & Zhang, W. (2019). *3D numerical simulation of wave transmission for low-crested and submerged breakwaters*. Coastal Engineering, 152, 103517.
https://doi.org/10.1016/j.coastaleng.2019.103517

29- Musa, M. A., Maliki, A. Y., Ahmad, M. F., Sani, W. N., Yaakob, O., & Samo, K. B. (2017). *Numerical simulation of wave flow over the overtopping breakwater for energy conversion (OBREC) device*. Procedia engineering, 194, 166-173. https://doi.org/10.1016/j.proeng.2017.08.131

30- Hydraulics Research Station (Great Britain). (1980). *Design of seawalls allowing for wave overtopping (Vol. 924)*. Hydraulics Research Station.

31- Ye, J., & Cao, D. (2026). *Spatial distribution of wave-by-wave overtopping behind coastal structures: a critical review of the literature and a novel semi-analytical model*. Coastal Engineering Journal, 68(1), 81-113. https://doi.org/10.1080/21664250.2026.2613601

32- Gholizadeh, S., Dezvareh, R., & Kiani, A. (2024). *Comparison of different support vector machine kernels for monitoring of the last decade of the Iranian part of eastern Caspian Lake*. International Journal Of Coastal, Offshore And Environmental Engineering (ijcoe), 9(1), 55-63.

33- Habib, M. A., Abolfathi, S., O'Sullivan, J. J., & Salauddin, M. (2025). *Improved predictive formulae for wave overtopping at sloped breakwaters using interpretable machine learning models*. Plos one, 20(12), e0337830.
https://doi.org/10.1371/journal.pone.0337830